Supplementary information for

Bio-Inspired Microneedles with Hierarchical Microchannels for Rapid Interstitial Fluid Collection and Analysis

Ge Li, Yang Yu, Zhenlong Meng, Dake Ai, Mingmin Li, and Yuanpeng Wang *

Tianjin Key Laboratory of Life and Health Detection, Life and Health Intelligent Research Institute, Tianjin University of Technology, Tianjin 300384, China

Email: wangyuanpeng@email.tjut.edu.cn (YW).

Table of contents:

Movie S1: Liquid in flat grooves.

Movie S2: Liquid flow in in hierarchical microchannel.

S1.1 Design of HMC-MNs patch

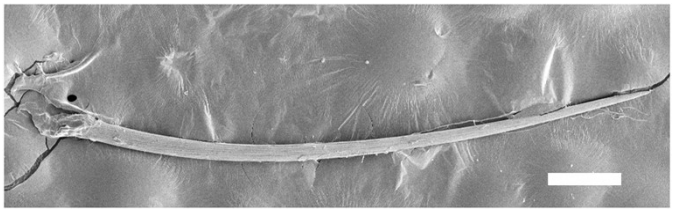

Fig. S1. SEM images of the *Sarracenia* trichome (scale bar: 0.2 mm).

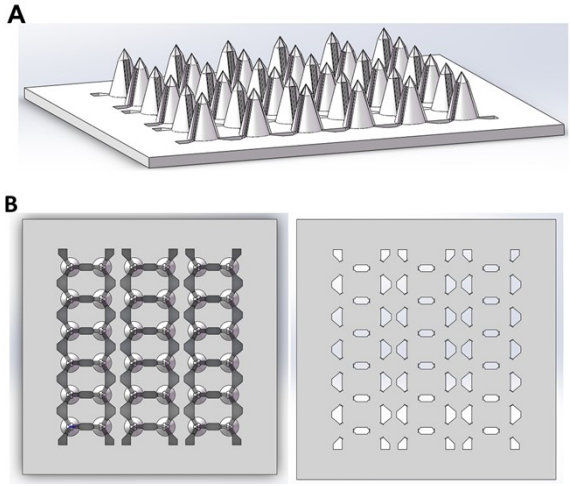

Fig. S2. Structural design drawings of the HMC-MNs patch. (A) Side view. (B) Vertical view.

S1.2 Fabrication and Characterization of HMC-MNs patch

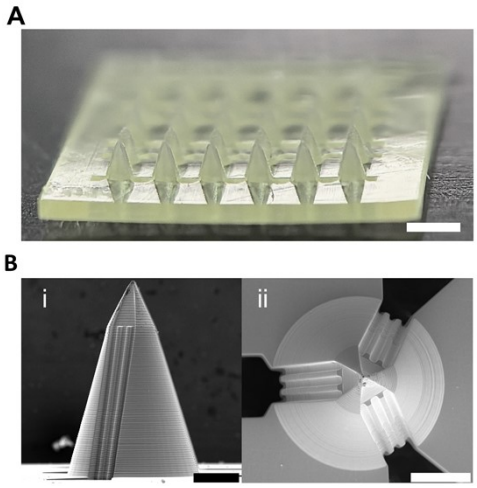

Fig. S3. The 3d printed HMC-MNs patch. (A) Optical images of the 3d printed HMC-MNs patch (scale bar: 1 mm). (B) SEM images of the 3d printed HMC-MN. (i) Side view, (ii) vertical view (scale bar: 200 μm).

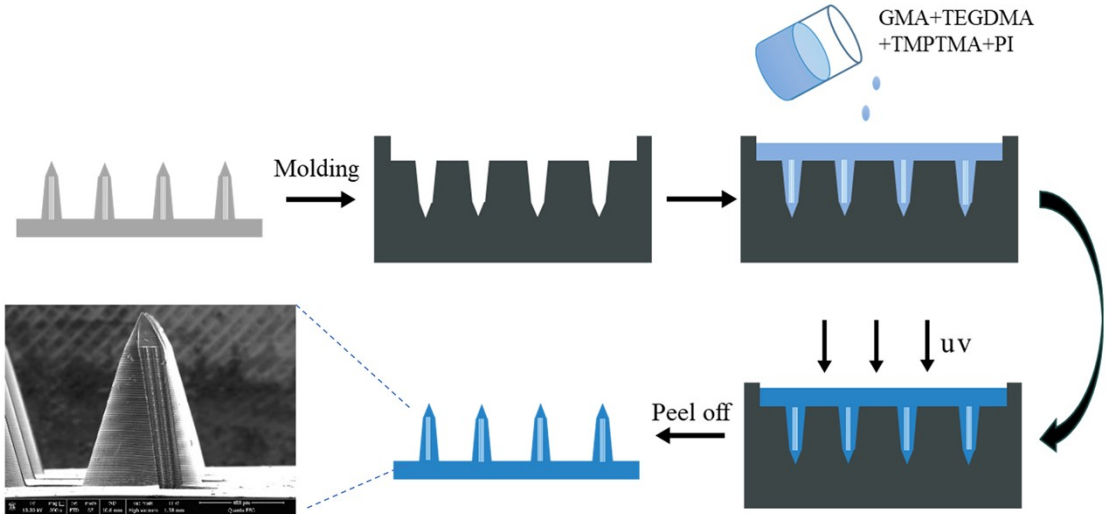

Fig. S4. Schematic of the fabrication process of the HMC-MNs patch.

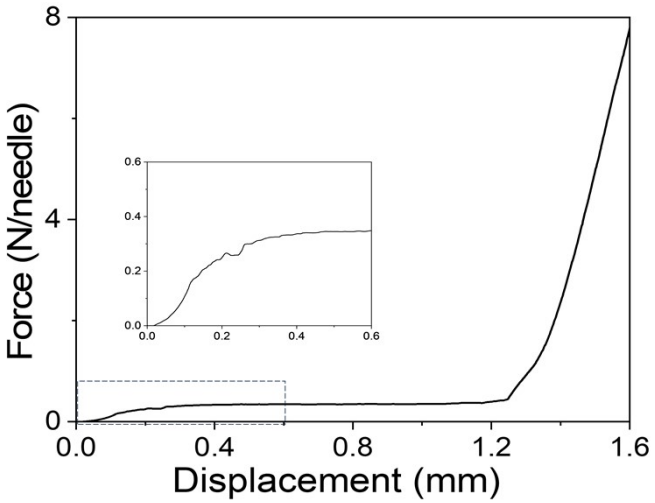

Fig. S5. Force-displacement curves of the 3d printed HMC-MNs in the mechanical compression test.

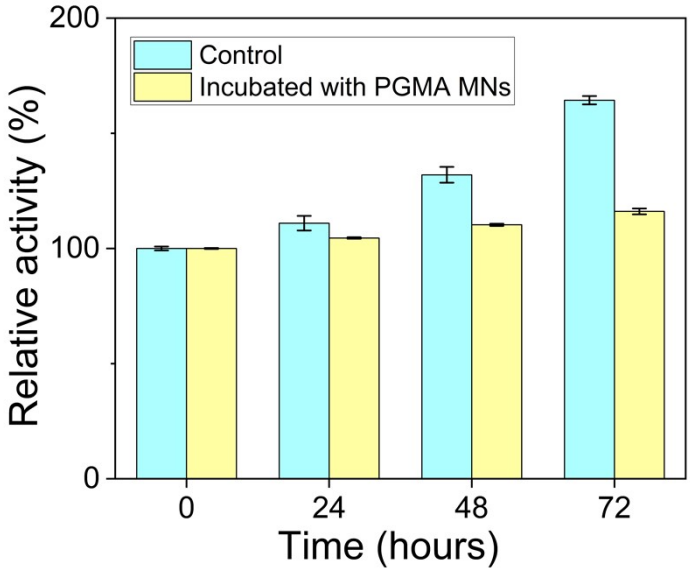

Fig. S6. Cytocompatibility of the PGMA HMC-MNs.

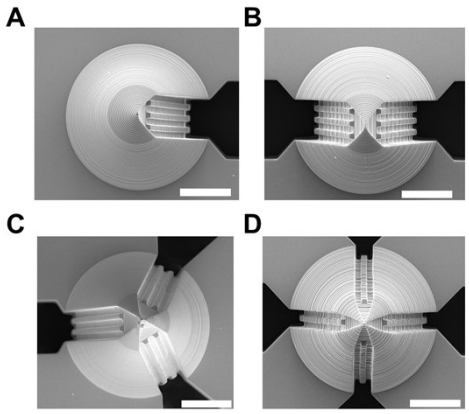

Fig. S7. SEM images of the 3d printed HMC-MN with various channels number per needle. (A) mono-, (B) di-, (C) tri-, and (D) tetra-grooved MN (scale bar: 200 μm).

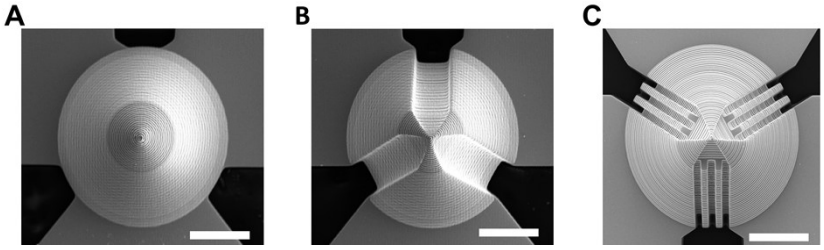

Fig. S8. SEM images of the 3d printed MNs with various surface structure. (A) SL-MN, (B) FG-MN, and (C) CG-MN (scale bar: 200 μm).

S1.3 Ex Vivo ISF Sensing and Analysis with HMC-MNs

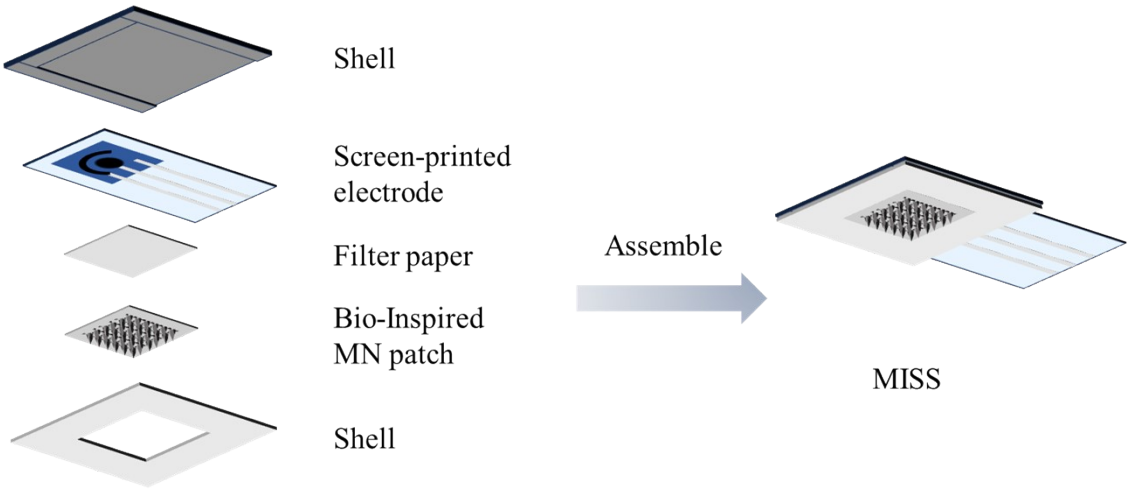

Fig. S9. Assembly diagram of MISS based on electrochemistry.

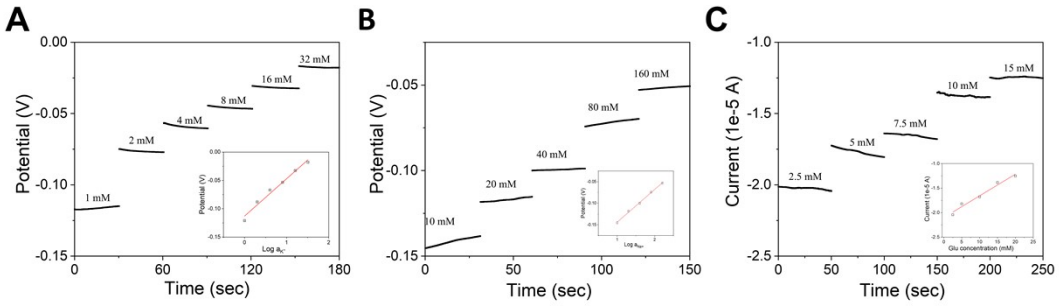

Fig. S10. Electrochemical performance of detection electrodes in MISS. Response of a K^+ (A), Na^+ (B), and glucose (C) detection electrode to various concentrations of biomarkers in artificial ISFs. Inset shows the Corresponding calibration curve.

S1.4 Evaluation of the HMC-MNs in ISF Extraction and Analysis in vivo

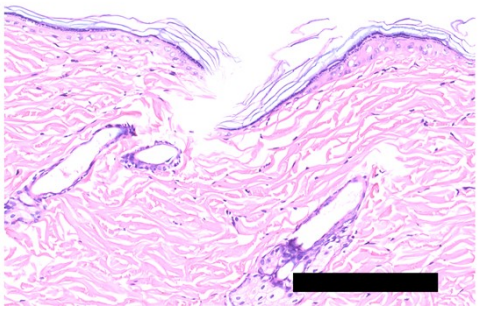

Fig. S11. H&E-stained sections of rat skin showing HMC-MNs penetration sites and the surrounding tissue.

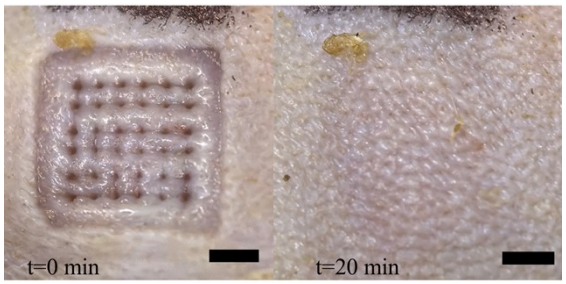

Fig. S12. Images of skin recovery after peeling off the HMC-MNs patch. (scale bar: 2 mm)

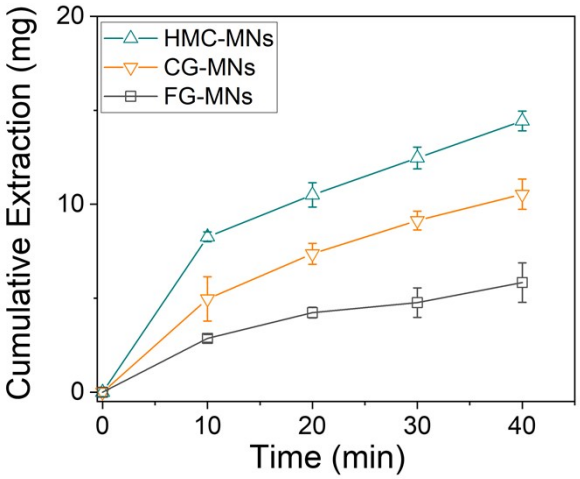

Fig. S13. ISF extraction experiment for MICS with various MNs on rat for 40 min.

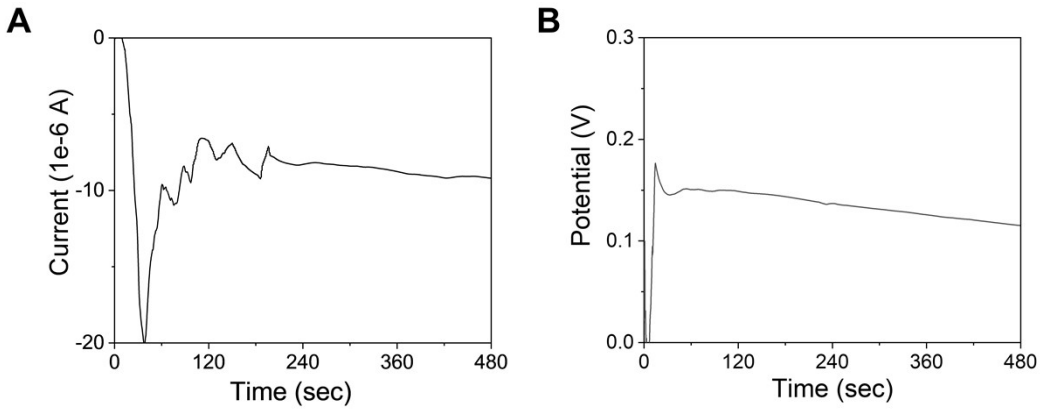

Fig. S14. The performance of the electrochemical MISS in vivo. (A) In vivo amperometric and OCPT responses for glucose and K^+ sensing in rats post-administration. The whole amperometric responses for glucose sensing in rats post-administration. (B) The whole OCPT for K^+ sensing in rats post-administration.

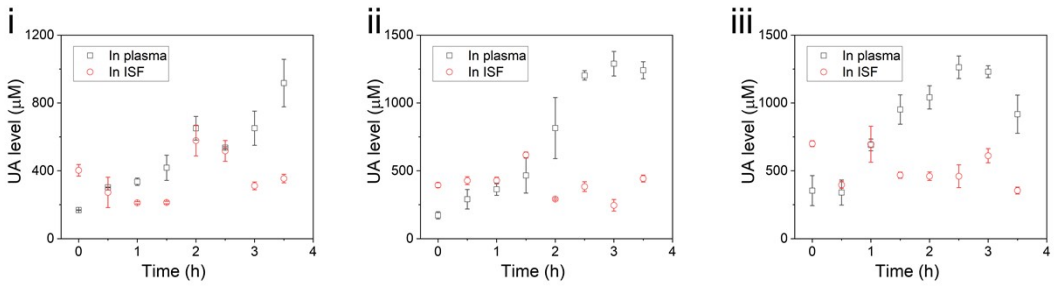

Fig. S15. Correlation of the UA concentrations measured in blood and extracted skin ISF on normal rats after a Potassium oxonate injection with various dosage.

S2 Further analysis for ISF flow on the MNs

S2.1 conditions under which the flow occurs inside the grooves

Upon penetration of the dermis by the microneedles (MNs), interstitial fluid (ISF) diffused into the grooves of the MNs from the surrounding tissue. The ISF subsequently flowed along the grooves, propelled by capillary forces. As reported in previous studies,[1] the capillary force F_{cap} driving fluid flow in an open groove can be expressed as:

$$F_{cap} = p_w \gamma \cos\theta - p_f \gamma \#(1)$$

where p_w is the wetting boundary on the flow cross-section (in contact with the groove wall), γ is the fluid surface tension θ is the fluid contact angle on the channel surface, and p_f is the air boundary on the flow cross-section (in contact with air).

Due to the fact that gravity can be ignored at the microscale, the prerequisite for flow to occur is that the driving force $F_{cap} > 0$,[2] that is :

$$\theta < \cos^{-1}\frac{p_f}{p_w} \#(2)$$

For the fluid in flat groove, the occurrence of flow requires the condition to be met:

$$\theta < \cos^{-1}\frac{p_f}{p_w} = cos^{-1}\frac{W}{2H+W} \#(3)$$

where W is the width of the rectangular groove section, and H is the depth of the groove section, as shown in Fig. S16. The flat grooves employed in this study had an aspect ratio of 0.33, a design that balanced the mechanical strength and replicability of the MNs, as demonstrated in Fig. 2B and 2C. At this aspect ratio, fluid flow requires a contact angle $\theta < 53.1°$, a threshold lower than the contact angles of most polymers suitable for fabricating solid MNs, including polymethyl methacrylate (PMMA), polycarbonate (PC), polystyrene (PS), cyclic olefin copolymers (COC), polyether ether ketone (PEEK), and poly(glycidyl methacrylate) (PGMA) used in this work.[3-6] Consequently, the capillary forces

generated were insufficient to drive ISF flow, as illustrated in Video S1. Instead, only minimal ISF entered the grooves, propelled by diffusion inertia, and was subsequently collected.

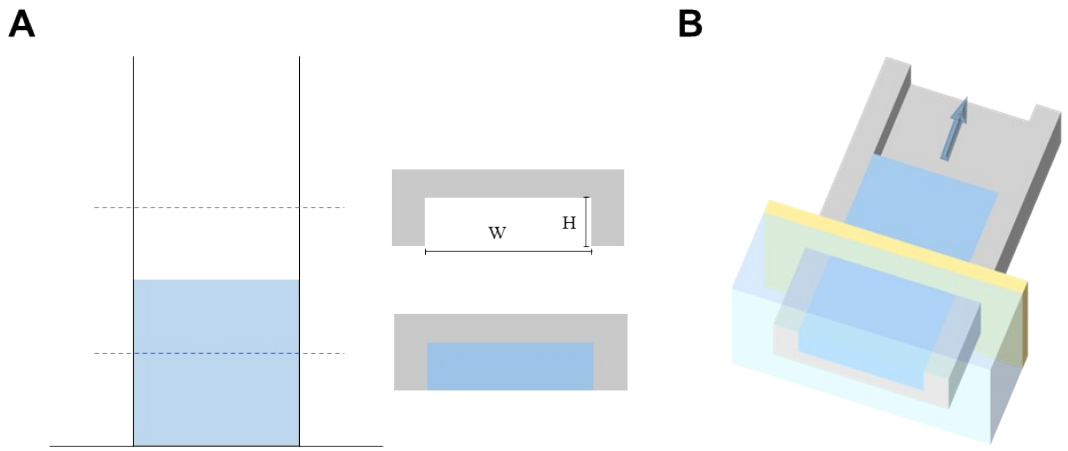

Fig. S16. Schematic models of liquid flow in flat grooves.

For the fluid in hierarchical microchannel (HMC), the fluid flow was divided into three parts: that in the step minor base microchannel (F1), the normal minor base microchannel (F2) and major microchannel (F3), as shown in Fig. S16.

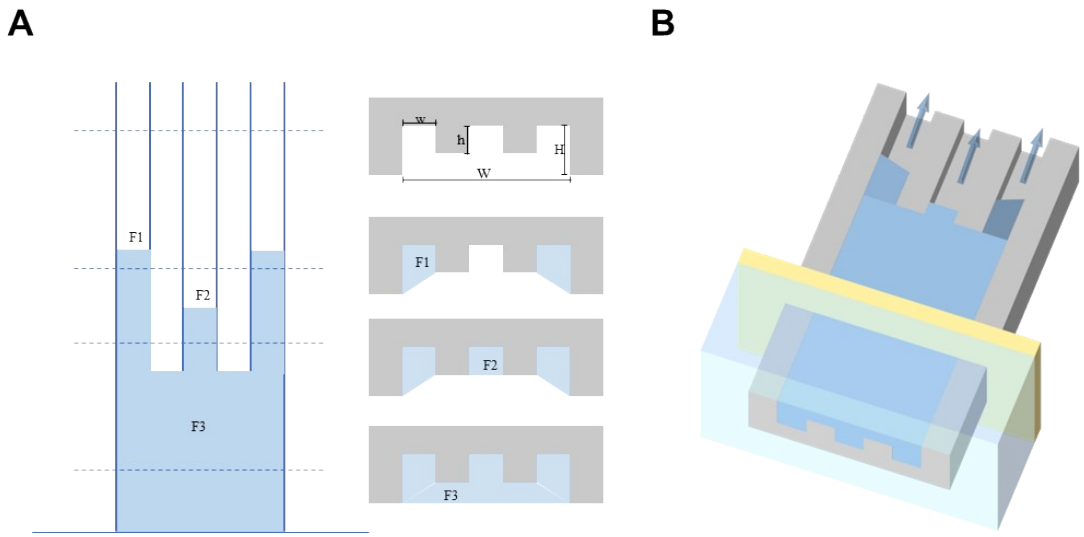

Fig. S17. Schematic models of liquid flow in in HMC.

For the fluid in the step minor base microchannel, the occurrence of flow requires the

condition to be met:

$$\theta < \cos^{-1}\frac{p_f}{p_w} = cos^{-1}\frac{\sqrt{(H-h)^2+w^2}}{H+h+w} \#(4)$$

where w is the width of the minor base microchannel, and h is the height of low ribs, as shown in Fig. S17. For the HMC design utilized in this study, fluid flow within the minor base microchannel required a contact angle $\theta < 70.9°$. The contact angle of PGMA, measured in a separate experiment as 65.7°, satisfied this criterion, indicating that flow within the microchannel would occur.

For the fluid in the normal minor base microchannel, the occurrence of flow requires the condition to be met:

$$\theta < \cos^{-1}\frac{p_f}{p_w} = cos^{-1}\frac{w}{2h+w} \#(5)$$

In the HMC design used in this study, fluid flow within the normal minor base microchannel required a contact angle $\theta < 70.5°$. This condition was met, confirming that flow would occur.

After the microchannels were filled with ISF, a major microchannel with a liquid film at its base was formed, as illustrated in Fig. S17A. Based on previous reports, the contact angle between identical fluids can be approximated as zero.[7] Consequently, analogous to liquid transport along the HMCs on the surface of *Sarracenia* trichomes,[7] the fluid in the major microchannel flowed in concert with the fluid in the minor base microchannel, as demonstrated in Video S2.

S2.2 Spontaneous Capillary flow inside the grooves

After the flow inside the groove occurred, the flow of ISF conformed to:

$$\frac{d(mv)}{dt} = F_{cap} - F_{drag} \#(6)$$

where m is the fluid mass in the channel, v is the fluid linear velocity, and F_{drag} is the frictional resistance. Due to the low Reynolds number of interstitial fluid,[8] friction depends on the geometry of the channel and fluid velocity:

$$F_{drag} = \frac{\mu v}{\bar{\lambda}} p_w l(t) \#(7)$$

Where μ is the viscosity of the ISF (similar to serum,[8] 0.0012 Pa.s), $\bar{\lambda}$ is the weighted friction length, and l(t) is the distance traveled by the fluid front in time t. Substituting equation (7) into equation (6) and accumulating points of the equation, we got modified Lucas Washburn formula[2] by Lee et al:

$$l(t) = \sqrt{\frac{\gamma}{\mu} 2\bar{\lambda} \cos\theta^*} \sqrt{t} \#(8)$$

where γ is the surface tension of ISF (similar to water,[8] 0.072 N/m at 37°C), θ^* is the weighted contact angle of the fluid, defined according to reference [1] as:

$$\cos\theta^* = \frac{-P_f + P_w \cos\theta}{P_w} \#(9)$$

According to reference,[2] for the fluid in flat groove:

$$F_{drag\ FG} \approx 6\mu \frac{v}{W} l(t)(2H) + 6\mu \frac{v}{H} l(t)(W) = 6\mu v\, l(t)\left(\frac{2H}{W} + \frac{W}{H}\right) \#(10)$$

Substituting equation (10) into equation (7) and accumulating points of the equation, we got:

$$\bar{\lambda}_{FG} = \frac{1W + 2H}{6\frac{2H}{W} + \frac{W}{H}} = 9.09\mu m \#(11)$$

According to equation (8), due to the weak hydrophilicity of the microchannel surface, it is difficult for ISF to flow through the groove and be collected by the MICS.

For the fluid in the step minor base microchannel of the HMC, θ^* and $\bar{\lambda}$ approximate match:

$$\cos\theta_{Stm}^{*} = \cos\theta - \frac{\sqrt{(H-h)^2 + w^2}}{H+h+w} = 0.084\#(12)$$

$$F_{drag\ Stm} \approx 6\mu\frac{v}{w}\,l(t)(H+h) + 6\mu\frac{v}{\frac{H+h}{2}}\,l(t)(w) = 6\mu v\,l(t)\left(\frac{H+h}{w} + \frac{2w}{H+h}\right)\#(13)$$

Substituting equation (13) into equation (7) and accumulating points of the equation, we got:

$$\bar{\lambda}_{Stm} = \frac{1 \quad w+H+h}{\frac{6H+h}{w} + \frac{2w}{H+h}} = 4.29\ \mu m\#(14)$$

Substituting equation (12) and equation (14) into equation (8), we got:

$$\frac{l_{Stm}(t)}{\sqrt{t}} \approx 6.57\ mm/\sqrt{s}$$

For the fluid in the normal minor base microchannel of the HMC, θ^{*} and $\bar{\lambda}$ match:

$$\cos\theta_{Nom}^{*} = \cos\theta - \frac{w}{2h+w} = 0.078\#(15)$$

$$F_{drag\ Nom} \approx 6\mu\frac{v}{w}\,l(t)(2h) + 6\mu\frac{v}{h}\,l(t)(w) = 6\mu v\,l(t)\left(\frac{2h}{w} + \frac{w}{h}\right)\#(16)$$

Substituting equation (16) into equation (7) and accumulating points of the equation, we got:

$$\bar{\lambda}_{Nom} = \frac{1w+2h}{\frac{62h}{w} + \frac{w}{h}} = 4\ \mu m\#(17)$$

Substituting equation (15) and equation (17) into equation (8), we got:

$$\frac{l_{Nom}(t)}{\sqrt{t}} \approx 6.13\ mm/\sqrt{s}$$

In the major microchannel of the HMC, the base microchannel was filled with ISF. As a result, the contact angle between the fluid in the major microchannel and that in the minor base microchannel could be approximated as 0°, effectively eliminating friction between

the two fluid layers.[7] Therefore, θ^* and $\bar{\lambda}$ approximate match:

$$\cos\theta_{Maj}^{*}=\frac{2\times\sqrt{(H-h)^2+w^2}+w+2w*\cos\theta-W}{2\times\sqrt{(H-h)^2+w^2}+3w}=0.075\#(18)$$

$$F_{drag\ Maj}\approx 6\mu\frac{v}{H-h}\,l(t)(2w)=12\mu v\,l(t)\left(\frac{w}{H-h}\right)\#(19)$$

Substituting equation (19) into equation (7) and accumulating points of the equation, we got:

$$\bar{\lambda}_{Maj}=\frac{1}{12}\frac{2\sqrt{(H-h)^2+w^2}+3w}{\frac{w}{H-h}}=7.20\ \mu m\#(20)$$

Substituting equation (18) and equation (20) into equation (8), we got:

$$\frac{l_{Maj}(t)}{\sqrt{t}}\approx 6.65\ mm/\sqrt{s}$$

Based on the above inference, ISF flow along the step minor base microchannel is expected to be faster than that along the normal minor base microchannel. Subsequently, ISF begins to flow along the major microchannel and spreads over the low ribs. While the flow velocity in the major microchannel is theoretically higher, this velocity is contingent on the complete filling of the corresponding normal minor base microchannel with ISF. This sequential flow behavior aligns with the experimental observations of ISF movement within the microchannels, as shown in Video S2.

For the fluid in the comb-shaped grooves, θ^* and $\bar{\lambda}$ approximate match:

$$\cos\theta_{CG}^{*}=\cos\theta-\frac{w}{2H+w}=0.181\#(21)$$

$$F_{drag\ CG}\approx 6\mu\frac{v}{w}\,l(t)(2H)+6\mu\frac{v}{H}\,l(t)(w)=6\mu v\,l(t)\left(\frac{2H}{w}+\frac{w}{H}\right)\#(22)$$

Substituting equation (22) into equation (7) and accumulating points of the equation, we got:

$$\bar{\lambda}_{Nom} = \frac{1w + 2H}{\frac{62H}{w} + \frac{w}{H}} = 4.41\ \mu m \#(23)$$

Substituting equation (21) and equation (23) into equation (8), we got:

$$\frac{l_{CG}(t)}{\sqrt{t}} \approx 9.78\ mm/\sqrt{s}$$

A comparison of ISF flow in the comb-shaped grooves versus the HMC reveals that the former exhibits greater flow propensity and higher velocity. However, the high aspect ratio (1.67) of the comb-shaped grooves poses significant fabrication challenges, compromising structural integrity, as illustrated in Fig. 3E. Blockages in the microchannels and the loss of ribs within the substrate pores impede ISF flow and reduce the number of functional microchannels available for transport.

S2.3 The flow inside the filter paper

Because the pore size of the filter paper is smaller than that of the microchannels, ISF flowing through the microchannels penetrates the filter paper under a stronger capillary force. Once in the filter paper, the ISF diffuses further, driven by the same capillary force. According to the Hagen–Poiseuille equation,[8] the ISF extraction rate is influenced by factors such as the viscosity and surface tension of ISF, the pore size and dimensions of the filter paper, the hydrophilicity of the filter paper matrix, and the effective contact area between the filter paper and the microchannels on the MN patch. Among these, the effective contact area is primarily determined by the MN structure. In FG-MNs, only limited and occasional contact occurs between the ISF and the filter paper within some grooves. In contrast, the HMC-MNs provide an effective contact area equivalent to the cross-sectional area of the HMC, which exceeds the cross-sectional area of the comb-shaped

grooves. However, structural issues such as rib loss and microchannel blockage restrict ISF infiltration to only a subset of the microchannels, further reducing the ISF extraction speed.

After several minutes of infiltration into the filter paper, the ISF extraction process became increasingly limited by the diffusion rate of ISF within the skin.[8] At this stage, the amount of ISF extracted by the CG-MNs gradually converged with that of the HMC-MNs, as illustrated in Fig. 3F and 5D.

S3 Supplementary Video Legends

Movie S1: Liquid in flat grooves. This video demonstrates the behavior of fluid within a flat groove on the surface of the FG-MN. When a drop of dye-labeled artificial ISF was introduced to the flat groove, it remained stationary within the groove and did not flow along its length.

Movie S2: Liquid flow in in HMC. This video simulates fluid behavior within a HMC on the surface of the MN. Upon contact with the HMC, a drop of dye-labeled artificial ISF first flows along the minor base microchannel. Once the minor base microchannel is filled, the fluid transitions to flow along the major microchannel.

References:

1. J. J. Lee, J. Berthier, A. B. Theberge and E. Berthier, *Langmuir*, 2019, **35**, 10667-10675.
2. J. Berthier, K. A. Brakke and E. Berthier, *Open microfluidics*, Scrivener Publishing, Beverly, Massachusetts, 2016.
3. H. Juster, B. van der Aar and H. de Brouwer, *Polymer Engineering & Science*, 2019, **59**, 877-890.
4. Y. Song, M. Dunleavy and L. Li, *ACS applied materials & interfaces*, 2023, **15**, 31092-31099.

5. F. Dawaymeh, Y. Abbas, M. Khaleel, A. Alazzam and N. Alamoodi, *Polymers (Basel)*, 2021, **13**, 2305.
6. L. Cassari, A. Zamuner, G. M. L. Messina, M. Marsotto, H. Chen, G. Gonnella, T. Coward, C. Battocchio, J. Huang, G. Iucci, G. Marletta, L. Di Silvio and M. Dettin, *Biomolecules*, 2023, **13**, 246.
7. H. Chen, T. Ran, Y. Gan, J. Zhou, Y. Zhang, L. Zhang, D. Zhang and L. Jiang, *Nature Materials*, 2018, **17**, 935-942.
8. P. P. Samant and M. R. Prausnitz, *Proceedings of the National Academy of Sciences*, 2018, **115**, 4583-4588.